



Stochastic reconstruction and electrical transport studies of porous cathode of Li-ion batteries

N. Siddique, Amir Salehi, Fuqiang Liu*

Electrochemical Energy Laboratory, Department of Materials Science and Engineering, University of Texas at Arlington, Arlington, TX 76019, USA

HIGHLIGHTS

- Nanoscale 3D Li-ion battery electrodes were numerically reconstructed.
- Intricate 3D battery architectures, randomness, and connectedness were detailed.
- The structure-level electric transport was studied on the reconstructed structures.
- Simulation data are compared favorably with the experimental results.
- The pore-level electrochemical transport study was attempted.

ARTICLE INFO

Article history:

Received 2 April 2012

Received in revised form

2 May 2012

Accepted 21 May 2012

Available online 13 June 2012

Keywords:

Li-ion battery

Electrode

Microstructure

Simulation

Reconstruction

ABSTRACT

The goal of this work is to study electrical transport within multiphase structures of Li-ion electrodes through numerical microstructure reconstruction and direct evaluation. Li-ion battery electrodes at different compositions were numerically reconstructed mimicking the experimental fabrication process. Electrode material agglomeration and interfaces between components, as well as possible implication on battery performance were explored. Distribution of electrode phases (active material particles, binder, conducting phase carbon), and electrical conductivity were studied upon the reconstructed 3D microstructure. The electrical conductivity of the electrodes was estimated from the reconstructed electrode structures, and compared favorably with those measured experimentally using four-probe tests. It has been found that macro mass transport properties of the numerically reconstructed electrodes depend critically on nanoscale physical characteristics of electrode components and their contact. This work revealed the localized nanoscale electrode complexity and transport processes in great details, which are currently difficult to investigate experimentally or by alternative models.

© 2012 Elsevier B.V. All rights reserved.

1. Introduction

High-capacity Li-ion batteries are among the most viable candidates for next generation, clean, and potentially fossil fuels independent electric vehicles. Extensive amount of research has already been devoted to improve the performance of the Li-ion batteries through developing electrode materials [1–5], reducing size [6] and optimizing shape [3,7,8] of the electrode particles, and using different additives [9–11]. Despite recent significant advances, sluggish species transport—both electrical and ionic—in a complex electrode architecture [12,13], as one of the main factors limiting Li-ion battery performance, has not been resolved. Fundamental understanding and quantitative

investigation of the electrochemical transport processes in a pore-level electrode microstructure, as key to resolve the sluggish transport, still remain elusive. The lack of detailed understanding has stagnated the development of the next generation Li-ion batteries.

The state-of-the-art experimental work has routinely relied on trial-and-error to obtain optimum battery electrode design parameters such as thickness, porosity [11,14], and composition [14]. With these parameters, performance of the battery could be widely varied as the conductivity of the electrode, and also the penetration of the electrolyte inside the porous electrode structure are altered. Prior work [15–23] has confirmed not only that localized microstructural phenomena are important, but also that interfacial interactions [24–28] are critical in predicting the ultimate performance and stability. Theoretical work of Li-ion batteries has focused on macroscopic models that do not address the localized phenomena at nanoscale [12,13,29–32]; therefore they are not

* Corresponding author. Tel.: +1 817 272 2704; fax: +1 814 272 2538.

E-mail address: fuqiang@uta.edu (F. Liu).

capable of addressing the intricate electrode details, randomness, and the effects that occur in 3D battery architectures. Furthermore, these localized phenomena cannot be properly accounted for in cell performance with equivalent circuit models [19,33–39]; nor can they be assessed with sufficient efficiency for simulation of large domains, using atomistic [40,41] or molecular dynamics [42–45] simulations. Microscopic modeling approach could be proven pivotal since the ignorance of electrode structure details has been a major impediment to investigating the processes occurring at the pore scale.

In this study, we expanded our previous fuel cell work on the process-based reconstruction algorithm and direct numerical simulation (DNS) approach [46] to study the Li-ion battery electrode architectures. LiFePO_4 cathode has been reconstructed numerically mimicking the experimental fabrication process. Detailed microstructure study and conductivity calculation have been performed on the reconstructed structures and compared with the experimental results. This approach aims to provide detailed insight into the localized nanoscale electrode complexity and transport processes, which are currently inaccessible experimentally or by existing macroscopic models. Battery evaluation of different electrodes was also performed to investigate their charge/discharge behavior.

2. Experimental

Electrodes containing Timcal Super P Li carbon, poly vinylidene fluoride (PVDF, Kynar, Elf-Atochem) as a binder, and active material LiFePO_4 were fabricated. The carbon-coated LiFePO_4 particles were synthesized in a solid-state synthesis route using two-step heat treatment up to 700 °C in argon atmosphere [47]. The active material, binder and carbon (corresponding to 10 wt%, 20 wt%, 30 wt%, and 40 wt%) were mixed thoroughly in 1-Methyl-2-Pyrrolidinone (NMP) to form a viscous ink. This ink

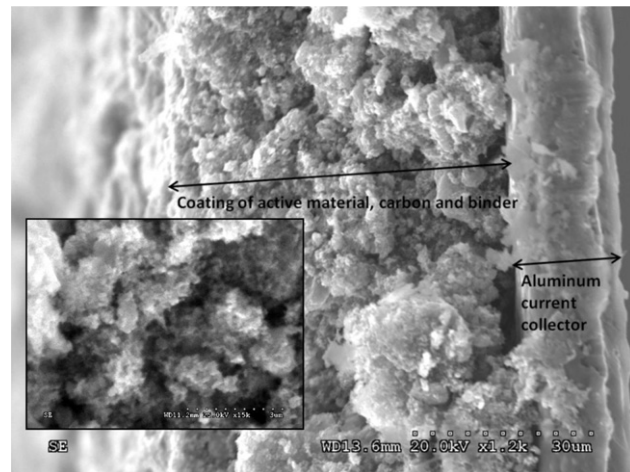


Fig. 1. SEM image of the cross section of a Li ion battery electrode (10% C, 10% binder, 80% LiFePO_4). The inset shows a high-magnification SEM image.

3. Simulation details

During numerical reconstruction, a controlled stochastic algorithm, elaborated in our earlier work [46], has been adopted to calculate the arrangement of each unit cell, i.e., location and layering sequence of certain component within a computational domain. An electrode segment of 500 nm × 250 nm × 250 nm was reconstructed using unit cells with dimension of 5 nm × 5 nm × 5 nm (totally 0.25 million unit cells). Each unit cell is assigned to a unique phase function, $f(i,j,k)$, representing a unique component in the electrode, e.g., binder ($f(i,j,k) = 2$), carbon ($f(i,j,k) = 1$), active material ($f(i,j,k) = 2$), and pore ($f(i,j,k) = 0$). As shown in Fig. 2, reconstruction starts with nucleation or seed, i.e.,

$$\mathbf{A} = \{ \dots; \underbrace{\text{cell}(i_1, j_1, k_1), \text{cell}(i_1, j_1, k_1) \dots}_{1, 2, \dots, p(i_1, j_1, k_1)}; \underbrace{\text{cell}(i_2, j_2, k_2), \text{cell}(i_2, j_2, k_2) \dots}_{1, 2, \dots, p(i_2, j_2, k_2)}; \underbrace{\text{cell}(i_3, j_3, k_3), \text{cell}(i_3, j_3, k_3) \dots}_{1, 2, \dots, p(i_3, j_3, k_3)} \dots \} \quad [1]$$

was coated on top of a polyether ether ketone (PEEK) film using a doctor blade, and then dried in a vacuum oven at 120 °C overnight. Fig. 1 shows the cross-sectional SEM image of battery electrodes with 10 wt% carbon additives. Total pore volume of the electrodes was evaluated by isopropyl alcohol (IPA) impregnation. Electrode samples were immersed in IPA solution for 4 h, and then taken out for weight measurement after wiping out the IPA at the electrode surface. The porosity of the electrode was calculated according to the weight gain due to IPA impregnation. The electrical conductivity of the electrode was measured by the four-probe measurement. Thickness of the electrodes was measured from cross-sectional SEM images. Pt or Cu wires with 1 cm distance were used. DC currents ranging between 1 and 5 mA were increased step-wise and the potential measured at the two inner probes was used to calculate the conductivity.

Battery performance was evaluated at room temperature in a homemade pouch cell, with lithium foil as negative electrode and coated LiFePO_4 on Al foil as positive electrode. All the cells contained 1.0 M LiPF_6 in EC–DMC (1:1 by volume) as electrolyte and were assembled in an argon-filled glove box. Charge and discharge characteristics were performed between 2.5 and 4.0 V using a multi-channel battery tester from MTI Corp.

randomly choosing seeds within the reconstruction domain for subsequent growth, and then followed by “growing” materials sequentially. At each growth step, a probability density function ($p(i,j,k)$), which is the number of neighboring “grown” cells is computed for each empty cell in the microstructure. Then a probability space, \mathbf{A} , is constructed as Eq. (1) shows, where cell (i,j,k) is the identifier of an empty cell. Note that the frequency of cell (i,j,k) included in \mathbf{A} is its probability density function. Next, a stochastic process is to choose one cell ($B(i,j,k)$) from space \mathbf{A} , i.e., $B(i,j,k) \in \mathbf{A}$, as a new cell to be grown. The above process is repeated until the desired amount of grown materials is achieved. For electrode components that only form on the surface of other preformed phases (e.g., carbon coating on electrode materials), the probability space will only include the empty cells located at the surface.

This reconstruction approach provides an effective way to pinpoint the localized electrical transport properties at pore level, which can be also transferred into a structure-level electrical conductivity. According to Fick’s first law with an applied current density (J), the structure-level effective conductivity σ_e^a is derived as,

$$\sigma_e^a = J \cdot \Delta l / \Delta E_e \quad [2]$$

where Δl is the thickness of the reconstructed domain (horizontal direction in Fig. 2), and ΔE_e is the potential difference. The effective conductivity captures the collective information of localized

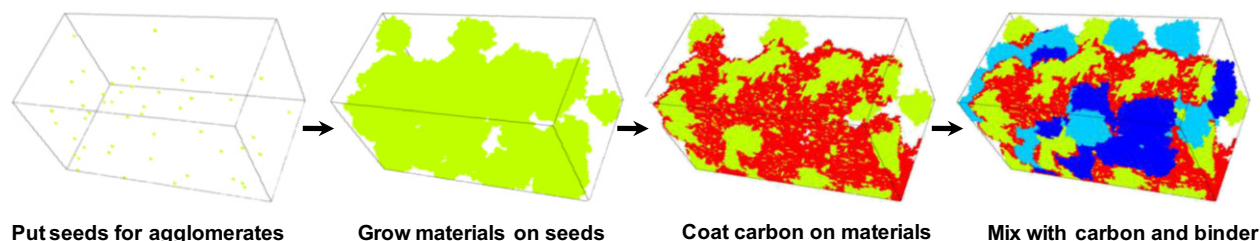


Fig. 2. Illustration of the numerical reconstruction process of Li-ion battery electrode in $500 \text{ nm} \times 250 \text{ nm} \times 250 \text{ nm}$. The electrode contains 7 wt% C, 7 wt% binder and 86 wt% active material with a porosity of 35%.

transport and strongly depends on the tortuosity and connectedness of the reconstructed structures. Fixed electrical potentials were applied at the front and back boundaries, e.g., 0 and 1V, respectively. The electrical current under this potential gradient was determined by running a full 3D simulation in a commercial computational fluid dynamic (CFD) software Fluent 6.3.26 and used to calculate the electrical conductivity according to Eq. (2). Thus, a direct numerical evaluation of material and structure transport properties of various designs is possible.

4. Results and discussion

Li-ion electrodes of several compositions (10 wt% C, 20 wt% C, 30 wt% C, and 40 wt% C) have been numerically reconstructed. The parameters used for the reconstruction are given in Table 1. The electrical conductivity of the Super P Li Carbon is estimated to be around 300 m/s which is close to that of carbon nanotube yarns [48]. Fig. 3 shows the four reconstruction trials of the electrode microstructures with 10 wt% carbon additive, 10 wt% binder, 80 wt% of LiFePO_4 , and a porosity of 40% measured by IPA impregnation. Three-dimensional microstructures of the electrodes clearly show the components such as LiFePO_4 , carbon coating on the LiFePO_4 particles, carbon additives, binder, and pores. Careful comparison between the numerically reconstructed nanostructure in Fig. 3 and the SEM image in Fig. 1 suggests close similarity. Both images indicate a random structure with irregular-shaped agglomerates of LiFePO_4 , PVDF binder, and carbon additives. The dark areas in the SEM image are voids between the agglomerates and the size is ranging from tens to hundreds of nanometers. The numerically reconstructed structures have similar agglomerate size, pore size and morphology. The reconstructed electrode architecture is also consistent with the observation in the experimental literature, for

example, Fig. 5 in reference [49], Fig. 8 in reference [50], and Fig. 5c in reference [51].

Cross-sectional microstructures of the electrodes (10% C, 10% binder, and 80% LiFePO_4), in x - z and y - z planes from the four different trials (Fig. 3), are shown in Fig. 4. It is clear that the LiFePO_4 particles have a thin layer of carbon coating connected to the network of carbon additives. The cross-sectional microstructures also show that there are several isolated islands of carbon additives separated by nonconductive binders. These islands are not connected to the main carbon network, therefore will not contribute to the electrical conductivity.

Fig. 5 shows the typical reconstructed electrode structures with 20 wt%, 30 wt%, and 40 wt% carbon additive. Structures from only one reconstruction trials are shown. Since the reconstructed domain automatically tracks the interfaces between different components, e.g., particle and carbon additive, and their interfaces, the phase connectivity, particle surfaces, and effective reaction interface within the battery electrode can be directly accessed from the reconstructed microstructure. Such a statistical analysis can thus provide important information on both transport and reaction processes resulted from structural and compositional variations, e.g., weight fraction of carbon additives.

The impact of carbon weight fraction is two-fold. *First*, LiFePO_4 particle agglomeration varies with fraction of carbon additives. At a constant nucleation number, i.e., 15, dispersion of LiFePO_4 particles only relies on the amount of active materials which reduce with increasing carbons in a fixed reconstruction volume. It is seen from the reconstructed structures in Fig. 5 that higher fractions of carbon additives result in smaller particle size. Though the primary particle size of LiFePO_4 is around 50–80 nm, its agglomeration leads to size of 200–300 nm as shown in Fig. 4. *Second*, LiFePO_4 agglomeration impacts interfacial area between different phases. For example, the interface between the active materials (with or without carbon coating) and carbon additives, which is critical to electron conduction within the electrode, depends on agglomeration of active materials and distribution of carbons. LiFePO_4/C interface is the most active due to highly conductive carbon additives; $\text{LiFePO}_4/\text{electrolyte}$ is the least active due to low conductivity of LiFePO_4 . This is because the electrical conductivity of carbon coating is 2–3 order of magnitude lower than carbon additives [52]. Surface reaction in Li-ion batteries relied on how fast the electrons can be supplied or removed from the particle surface.

Distributions of interfacial area between LiFePO_4 in the typical reconstructed electrodes at different compositions are plotted in Fig. 6. High carbon fractions, i.e., 30 wt% and 40 wt%, create noticeable interface discontinuity (zero interfacial area section) along the thickness; while in comparison, reducing carbon amount tends to improve the interfacial distribution along the electrode thickness. Moreover, the interfacial area per unit mass of LiFePO_4 increases with the carbon weight fraction as clearly demonstrated in Fig. 6. The averaged interfacial area per unit mass of LiFePO_4 first

Table 1
List of parameters used in the numerical reconstruction of the electrodes.

Parameter	Value
Electrical conductivity of Super P Li Carbon	300 S/m
Electrical conductivity of active material LiFePO_4 [54]	1×10^{-7} S/m
Electrical conductivity of carbon coating on active material [54]	1×10^{-4} S/m
Percent of carbon in the coating of the active material particles	8%
Porosity of added Super P Li carbon	85%
Density of carbon	2.2 g/cm ³
Density of active material LiFePO_4 [54]	3.6 g/cm ³
Density of binder (PVDF) [55]	1.76 g/cm ³
Number of LiFePO_4 nucleation sites	15
Number of carbon coating nucleation sites	50
Number of binder nucleation sites	15
Number of added carbon nucleation sites	25

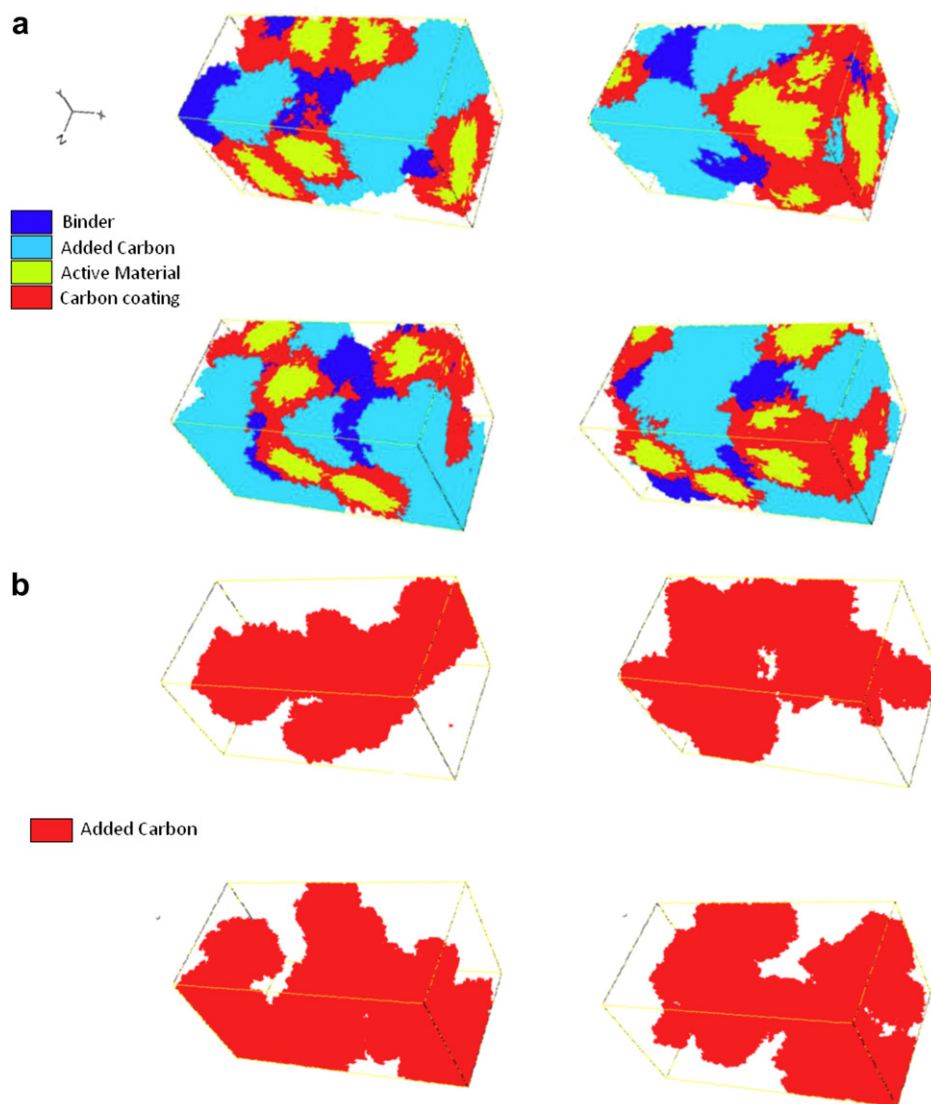


Fig. 3. Numerical reconstruction of Li-ion battery electrode containing 10% C, 10% binder and 80% active material with a porosity of 40%: (a) Microstructure of electrode, and (b) carbon distribution.

increases from $13.61 \text{ m}^2/\text{g}$ at 10 wt% carbon to $30.1 \text{ m}^2/\text{g}$ at 20 wt% carbon, and then stabilizes at around $60 \text{ m}^2/\text{g}$ when the carbon weight fraction increases to 30 and 40 wt%. This shows that interfacial area and therefore macro-homogeneous electrode characteristics rely on the localized electrode structure and particle agglomeration, which serves as a design consideration for better activity and durability. This different surface coverage will have a significant impact on both reaction kinetics and electrode electrical conductivity, and therefore the discharge capacity.

Figs. 3b and 5b shows arrangement of carbon additives in the simulation domains where a continuous electron transport path along the thickness of the electrode (normalized x direction in the image) can be easily identified, although at some points carbon necks appear. These necks act as electron transport barriers and will contribute to conductivity loss. When the carbon fraction increases to 20%, 30%, and 40%, this connectivity increases which ensures the electrons supplied to the LiFePO_4 particles during the electrochemical reaction. This can be seen with the distribution of carbon throughout the thickness of the electrode in Fig. 7. Results of only one typical reconstruction trial have been plotted for each carbon fraction. Fig. 7 shows that there is a neck of carbon

connection in the electrode containing 10% C where carbon volume fraction is close to zero. Increasing carbon fraction in the electrode reduces the probability of neck formation and ensures a continuous path of electron transport, and therefore probably better electrical conductivity.

Fig. 8 shows the effective electrical conductivity vs. carbon weight fraction averaged out of 8 reconstruction trials. Electrical conductivity was calculated according to Eq. (2). It is believed that a domain size containing more than 20–50 electrode particles as shown in Figs. 2–5 (corresponding to particle size in the range of 20–100 nm) is sufficient to achieve a realistically representative electrode macro properties, assuming there are no major structural defects. The experimentally measured conductivity value is also displayed in Fig. 8. The results show a good agreement between the experimental and simulated values. Conductivity clearly showed an increasing trend with carbon fraction.

Fig. 9 shows the battery discharge performance of the electrodes with different carbon contents. The discharge potential is similar for different carbon fractions at the beginning of the two phase transition region; however, it starts to deviate from each other along the discharging process. Though the capacities of the

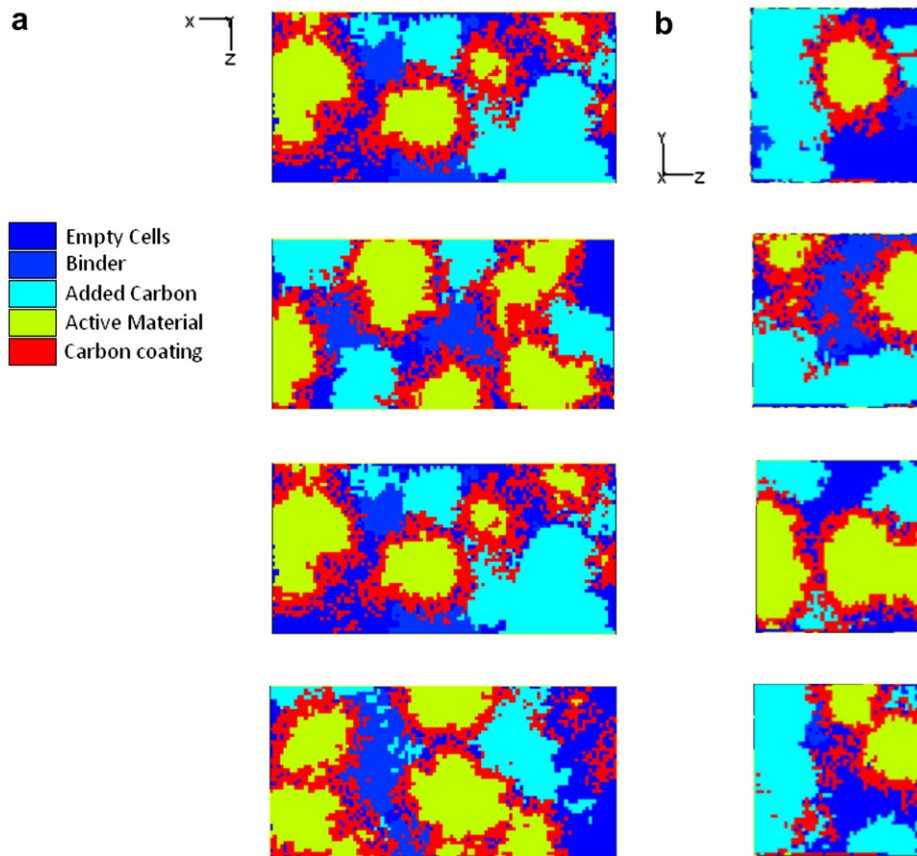


Fig. 4. Cross sections of electrodes containing 10% C, 10% binder and 80% active material with 40% porosity. (a) X–Z mid-planes, and (b) Y–Z mid-planes.

electrodes seem low (the main purpose of this study is not to optimize battery performance), there exists a clear trend that increasing carbon content improves battery capacity. From 10 wt % C to 40 wt% C, the battery discharge capacity increases from 93 to

125 mAh/g at 0.1 C, as a result of the strong effect of electrode conductivity on battery discharge capacity [53]. It is well-known that both electronic and ionic conductivities are critical to the cathode behavior of a Li-ion battery. However, the IPA impregnation measurement gave similar electrode porosities—around 40%—for the four electrodes with different carbon weight fractions in our study. This porosity translates to an almost identical effective ionic conductivity within the electrodes, i.e., 0.28 S/m, for the four

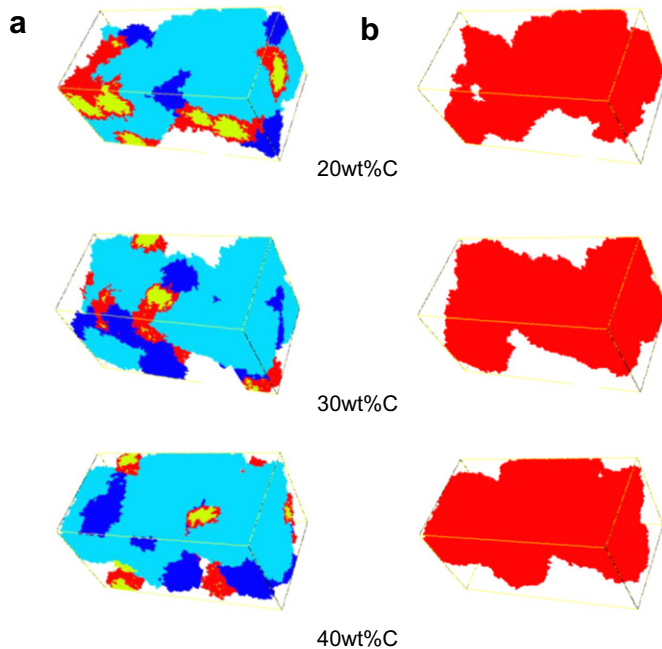


Fig. 5. Influence of electrode composition (amount of carbon additives) on electrode microstructure: (a) Microstructure of electrode, and (b) carbon distribution.

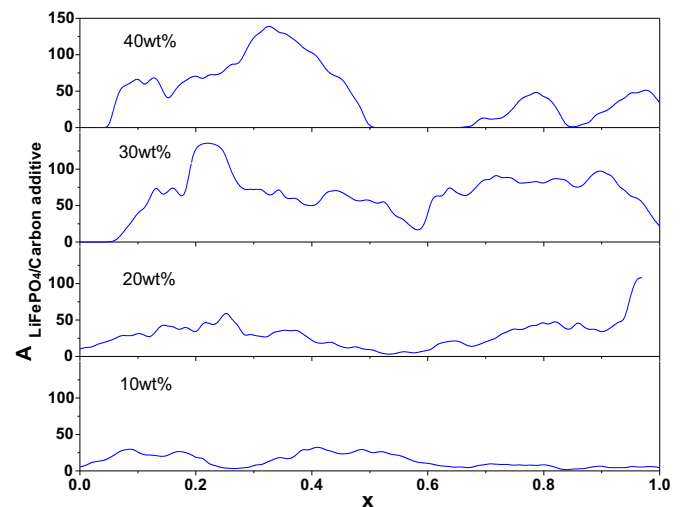


Fig. 6. Distribution of interfacial area between LiFePO₄ and carbon additives along the thickness of the reconstructed Li-ion electrodes.

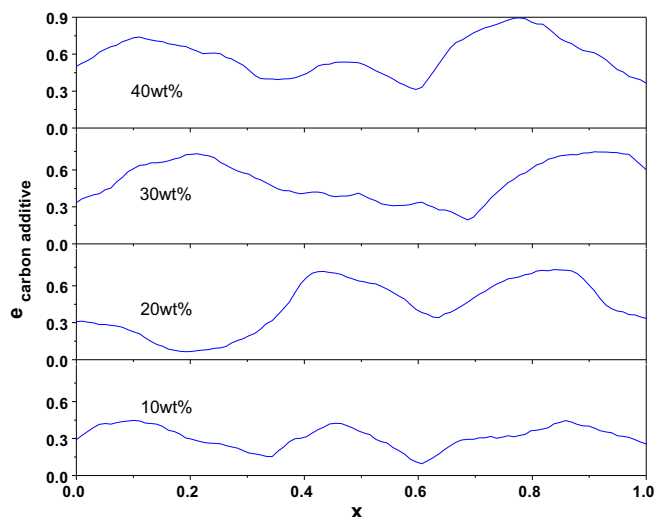


Fig. 7. Volume fractions of transport carbon throughout the thickness of the reconstructed electrodes.

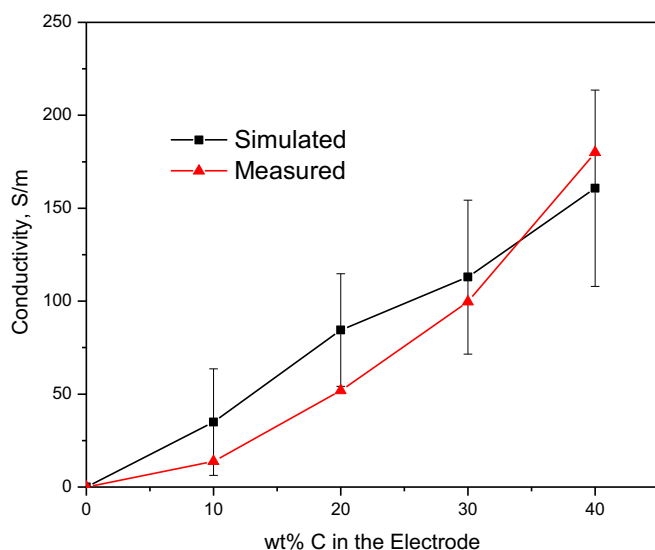


Fig. 8. Conductivity of the electrodes with the variation of composition.

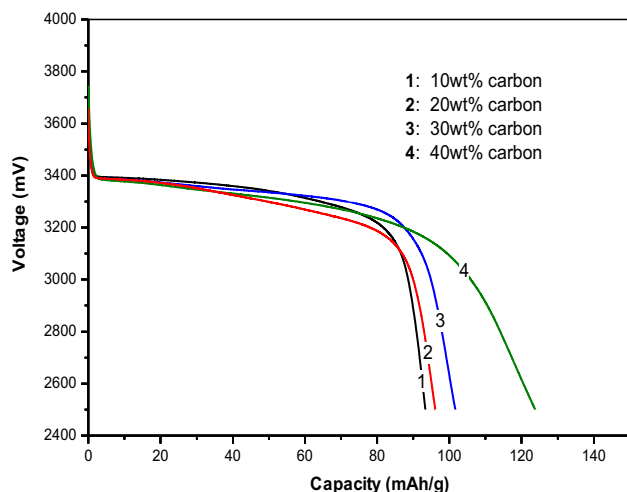


Fig. 9. Li-ion battery discharge performance with electrodes of different compositions at 0.1 C.

electrode compositions using Bruggeman's correction. Therefore, it seems that the observed increase of battery discharge capacity results only from a combined effect of improved electrode conductivity as well as interfacial contact between active materials and carbon additives, as clearly demonstrated in Figs. 6 and 8, respectively.

5. Conclusion

Li-ion battery electrodes of different compositions have been numerically reconstructed to study the nanoscale three-dimensional microstructure and distribution of the components throughout the electrode. The electrical conductivity of the electrodes was evaluated from the reconstructed electrode structures, and compared favorably with those measured experimentally using four-probe tests. It has been found that macro mass transport properties of the numerically reconstructed electrodes depend critically on nanoscale physical characteristics of electrode components and their contact. The reconstructed multiphase structures helps to optimize the fabricating parameters of the electrode (porosity, composition, extent of mixing of components before coating etc). The approach developed in this work thus offers a direct numerical evaluation of transport properties in structures of various designs.

Acknowledgments

This work was financially supported by National Science Foundation ECCS-1125588. This work is also partially supported by UTA Research Enhancement Project 14-7488-59. F.L. wants to acknowledge the support from the faculty startup fund of University of Texas at Arlington.

References

- [1] J. Akimoto, Y. Gotoh, Y. Oosawa, *Journal of Solid State Chemistry* 141 (1998) 298–302.
- [2] I. Belharouak, D. Vissers, K. Amine, *Journal of the Electrochemical Society* 153 (2006) A2030–A2035.
- [3] P.P. Mukherjee, *Journal Name: Electrochemical and Solid-State Letters; Journal Volume: 14; Journal Issue: 10, Medium: X; Size: A143–A147.*
- [4] F. La Mantia, F. Rosciano, N. Tran, P. Novák, *Journal of Applied Electrochemistry* 38 (2008) 893–896.
- [5] T. Thongtem, S. Thongtem, *Inorganic Materials* 42 (2006) 202–209.
- [6] K.T. Nam, D.W. Kim, P.J. Yoo, C.Y. Chiang, N. Meethong, P.T. Hammond, Y.M. Chiang, A.M. Belcher, *Science* 312 (2006) 885–888.
- [7] Z. Wang, S. Su, C. Yu, Y. Chen, D. Xia, *Journal of Power Sources* 184 (2008) 633–636.
- [8] B.-J. Hwang, K.-F. Hsu, S.-K. Hu, M.-Y. Cheng, T.-C. Chou, S.-Y. Tsay, R. Santhanam, *Journal of Power Sources* 194 (2009) 515–519.
- [9] J. Humberto, D.K. Thomas, Z. Karim, P. Jai, *Journal of the Electrochemical Society* 156 (2009) A401–A406.
- [10] Y. Jingsi, X. Jun John, *Electrochemical and Solid-State Letters* 7 (2004) A515–A518.
- [11] Y.H. Chen, C.W. Wang, G. Liu, X.Y. Song, V.S. Battaglia, A.M. Sastry, *Journal of the Electrochemical Society* 154 (2007) A978–A986.
- [12] P. Albertus, J. Christensen, J. Newman, *Journal of the Electrochemical Society* 156 (2009) A606–A618.
- [13] M. Doyle, J. Newman, A.S. Gozdz, C.N. Schmutz, J.M. Tarascon, *Journal of the Electrochemical Society* 143 (1996) 1890–1903.
- [14] H. Meng, F. Xie, J. Chen, P.K. Shen, *Journal of Materials Chemistry* 21 (2011) 11352–11358.
- [15] P.L. Moss, G. Au, E.J. Plichta, J.P. Zheng, *Journal of the Electrochemical Society*, 157 A1–A7.
- [16] Q. Zhang, R.E. White, *Journal of Power Sources* 179 (2008) 793–798.
- [17] Z.H. Chen, K. Amine, *Journal of the Electrochemical Society* 153 (2006) A316–A320.
- [18] R. Chandrasekaran, G. Sikha, B.N. Popov, *Journal of Applied Electrochemistry* 35 (2005) 1005–1013.
- [19] B.Y. Liaw, R.G. Jungst, G. Nagasubramanian, H.L. Case, D.H. Doughty, *Journal of Power Sources* 140 (2005) 157–161.
- [20] A.T. Stamps, C.E. Holland, R.E. White, E.P. Gatzke, *Journal of Power Sources* 150 (2005) 229–239.
- [21] Z.Y. Tang, Y.L. Ruan, *Progress in Chemistry* 17 (2005) 1–7.

- [22] G. Sikha, B.N. Popov, R.E. White, *Journal of the Electrochemical Society* 151 (2004) A1104–A1114.
- [23] S. Ahn, Y. Kim, K.J. Kim, T.H. Kim, H. Lee, M.H. Kim, *Journal of Power Sources* 81 (1999) 896–901.
- [24] D. Zhao, Q. Huang, X.B. Jin, X.J. Wei, G.Z. Chen, *Acta Physico-Chimica Sinica* 26 (2010) 1239–1248.
- [25] K. Xu, A. von Cresce, U. Lee, *Langmuir* 26 (2010) 11538–11543.
- [26] V.A. Sethuraman, L.J. Hardwick, V. Srinivasan, R. Kostecki, *Journal of Power Sources* 195 (2010) 3655–3660.
- [27] B. Baek, C. Jung, *Electrochimica Acta* 55 (2010) 3307–3311.
- [28] J.A. Choi, S.M. Eo, D.R. MacFarlane, M. Forsyth, E. Cha, D.W. Kim, *Journal of Power Sources* 178 (2008) 832–836.
- [29] R. Darling, J. Newman, *Journal of the Electrochemical Society* 145 (1998) 990–998.
- [30] M. Doyle, T.F. Fuller, J. Newman, *Electrochimica Acta* 39 (1994) 2073–2081.
- [31] G.G. Botte, R.E. White, *Journal of the Electrochemical Society* 148 (2001) A54–A66.
- [32] G.G. Botte, V.R. Subramanian, R.E. White, *Electrochimica Acta* 45 (2000) 2595–2609.
- [33] N. Ariel, G. Ceder, D.R. Sadoway, E.A. Fitzgerald, *Journal of Applied Physics* 98 (2005).
- [34] Y. Zhang, Y.W. Liu, Y.S. Cheng, X.G. Hu, *Journal of Central South University of Technology* 12 (2005) 309–314.
- [35] B.Y. Liaw, G. Nagasubramanian, R.G. Jungst, D.H. Doughty, *Solid State Ionics* 175 (2004) 835–839.
- [36] S. Abu-Sharkh, D. Doerffel, *Journal of Power Sources* 130 (2004) 266–274.
- [37] I. Bloom, S.A. Jones, E.G. Polzin, V.S. Battaglia, G.L. Henriksen, C.G. Motloch, R.B. Wright, R.G. Jungst, H.L. Case, D.H. Doughty, *Journal of Power Sources* 111 (2002) 152–159.
- [38] Y.C. Chang, J.H. Jong, G.T.K. Fey, *Journal of the Electrochemical Society* 147 (2000) 2033–2038.
- [39] S.R. Narayanan, D.H. Shen, S. Surampudi, A.I. Attia, G. Halpert, *Journal of the Electrochemical Society* 140 (1993) 1854–1861.
- [40] J.N. Reimers, *Journal of Power Sources* 54 (1995) 16–19.
- [41] C.Y. Ouyang, S.Q. Shi, Z.X. Wang, X.J. Huang, L.Q. Chen, *Physical Review B* 69 (2004).
- [42] O. Borodin, G.D. Smith, P. Fan, *The Journal of Physical Chemistry B* 110 (2006) 22773–22779.
- [43] S.H. Garofalini, *Journal of Power Sources* 110 (2002) 412–415.
- [44] K. Moriguchi, S. Munetoh, M. Abe, M. Yonemura, K. Kamei, A. Shintani, Y. Maehara, A. Omaru, M. Nagamine, *Journal of Applied Physics* 88 (2000) 6369–6377.
- [45] M.E. Garcia, E. Webb, S.H. Garofalini, *Journal of the Electrochemical Society* 145 (1998) 2155–2164.
- [46] N.A. Siddique, F. Liu, *Electrochimica Acta* 55 (2010) 5357–5366.
- [47] S.-Y. Chung, J.T. Bloking, Y.-M. Chiang, *Nature Materials* 1 (2002) 123–128.
- [48] M. Zhang, K.R. Atkinson, R.H. Baughman, *Science* 306 (2004) 1358–1361.
- [49] M. Maccario, L. Croguennec, F. Weill, F. Le Cras, C. Delmas, *Solid State Ionics* 179 (2008) 2383–2389.
- [50] S.-T. Myung, S. Komaba, N. Hirosaki, H. Yashiro, N. Kumagai, *Electrochimica Acta* 49 (2004) 4213–4222.
- [51] W. Dreyer, J. Jamnik, C. Gohlke, R. Huth, J. Moskon, M. Gaberscek, *Nature Materials* 9 (2010) 448–453.
- [52] D.W. James, M.D. Marca, M. Marek, K. Robert, *Journal of the Electrochemical Society* 154 (2007) A389–A395.
- [53] W. Lu, S.-H. Kang, *Vehicle Technologies Annual Merit Review and Peer Evaluation*. Washington, D.C. (2009).
- [54] J.D. Wilcox, M.M. Doeff, M. Marcinek, R. Kostecki, *Journal of the Electrochemical Society* 154 (2007) A389–A395.
- [55] T. Marks, S. Trussler, A.J. Smith, D. Xiong, J.R. Dahn, *Journal of the Electrochemical Society*, 158 A51–A57.